Multiply Enhanced Odd-Order Wave-Mixing Spectroscopy

Nathan A. Mathew, Stephen B. Block, Lena A. Yurs, Kathryn M. Kornau, Andrei V. Pakoulev, and John C. Wright*

Department of Chemistry, University of Wisconsin Madison, Madison, Wisconsin 53706

Received: June 19, 2009; Revised Manuscript Received: September 11, 2009

Extending current coherent multidimensional spectroscopy (CMDS) methods to higher order multiwave mixing requires excitation intensities where dynamic Stark effects become important. This paper examines the dynamic Stark effects that occur in mixed frequency/time domain CMDS methods at high excitation intensities in a model system with an isolated vibrational state. The phase-matching restrictions in CMDS define the excitation beams that interact by nonlinear mixing while the dynamic Stark effects create vibrational ladders of increasingly more energetic overtone and combination band states. The excited quantum states form coherences that reemit the output beams. This paper uses the phase-matching conditions $\vec{k}_{\text{out}} = \vec{k}_1 - \vec{k}_2 + \vec{k}_{2'}$ and $\vec{k}_{\text{out}} = -\vec{k}_1 + \vec{k}_2 + \vec{k}_{2'}$, where the subscripts denote the excitation frequencies of each excitation pulse and the output pulse. The phase-matching condition constrains each pulse to have an odd number of interactions so the overall mixing process that creates the output coherence must also involve an odd number of interactions. Tuning the excitation frequencies and spectrally resolving the output intensity creates three-dimensional spectra that resolve the individual overtone states. Changing the excitation pulse time delays measures the dynamics of the coherences and populations created by the multiple excitations. The multidimensional spectra probe the highly excited states of a molecular potential energy surface. This paper uses tungsten hexacarbonyl ($W(CO)_6$) as a model for observing how dynamic Stark effects change the multidimensional spectra of a simple system. The simplicity of the $W(CO)_6$ system provides the experimental data required to develop the nonperturbative theoretical methods that will be necessary to model this new approach to CMDS.

Introduction

The selectivity of multiple pulse nuclear magnetic resonance (NMR) rests on its ability to excite multiple spin transitions to create coherent superposition states that are selective for specific molecules.[1−3] The multiple transitions must occur within the superposition state's dephasing time. Similarly, the development of the coherent optical analogues to multiple pulse NMR requires the ability to excite multiple optical transitions within the dephasing time of the coherent superposition states. Since dephasing rates for optical transitions are orders of magnitude faster than spin transitions, high excitation intensities are required to create Rabi frequencies that are comparable to the coherence dephasing rates. High intensities, however, create dynamic Stark effects, so it becomes important to understand how dynamic Stark effects change CMDS spectra. Dynamic Stark effects are commonly used to create the multiple interactions needed to generate highly excited state populations in pump−probe experiments and control reaction dynamics in coherent control experiments.[4−7] Chirped pulses[5] and temporally shaped pulses[7] are particularly effective in driving multiple interactions because the changing frequencies can match the changes in the anharmonicity of increasingly energetic states.

In this paper, we use $W(CO)_6$ as a model compound for exploring the effects of dynamic Stark effects on coherent multidimensional spectra. $W(CO)_6$ is a model compound because it has an isolated vibrational transition and a very large transition moment.[8−22] Thus, dynamic Stark effects can be obtained with modest excitation intensities and observed without competing effects from overlapping transitions. This paper describes a mixed frequency/time domain multiply enhanced odd-order wave-mixing (MEOW) approach where multiple beams and dynamic Stark effects coherently create a series of ladder-climbing excitations that populate highly excited states and probe their dynamics. The experiments demonstrate that this method can excite the $v = 6$ overtone of the symmetric stretch mode using 12 wave mixing. Three excitation pulses create coherent output beams by MEOW, and a monochromator spectrally resolves the output frequencies. The intensity of the first two excitation pulses is high enough to cause multiple interactions and climb the potential well using the dynamic Stark effects while the last pulse typically has a lower intensity and interacts a single time. Changing the excitation and monochromator frequencies allows measurement of the multidimensional spectra. Changing the time delays between the three excitation pulses allows measurement of the dynamics of the coherences and populations created by MEOW. The dynamic Stark effect broadens the transitions so even overtone states with large anharmonicities can be efficiently excited using excitation sources whose bandwidth would not normally cause a transition.

Theory

In a phenomenological description of multiwave mixing, the polarization of an isotropic system is written as a Taylor series expansion in the field

$$P \rightarrow \chi^{(1)}E + \chi^{(3)}E^3 + \chi^{(5)}E^5 + \cdots \tag{1}$$

since the even terms vanish by symmetry.[23] Each $\chi^{(n)}$ represents n electric field/matter interactions. Our experiment uses three discrete excitation pulses with two independently tunable

---

* To whom correspondence should be addressed. E-mail: wright@chem.wisc.edu.

10.1021/jp905796y CCC: $40.75

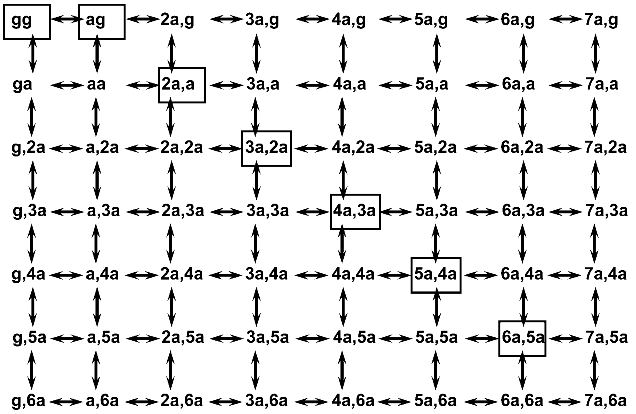

Figure 1. Liouville pathways for the multiply enhanced odd-wave mixing. The letters designate the density matrices describing the coherences and populations resulting from interaction with an electromagnetic field. The arrows are double headed because in the strong field limit, transitions can occur in either direction. Horizontal arrows correspond to ket-side transitions and vertical arrows correspond to bra-side arrows. Boxes denote the initial ground state population, *gg*, and the output coherences created with the $\vec{k}_4 = \vec{k}_1 - \vec{k}_2 + \vec{k}_{2'}$ phase-matching condition.

frequencies, ω_1 and ω_2. The ω_2 beam is split to create the third excitation pulse, $\omega_{2'}$. Under these conditions, $E = E_1 + E_2 + E_{2'}$. In coherent experiments, the nonlinear polarization represented by eq 1 is spatially coherent and emits beams in directions determined by the phase-matching condition. This technique allows weak nonlinear signals to be observed against stronger processes which emit in 4π steradians. The direction is determined by momentum conservation as defined by the *k*-vector addition of the interacting laser fields. The two phase matching conditions for the $\vec{k}_{\text{out}}$ output beam in our experiments are $\vec{k}_{\text{out}} = \vec{k}_1 - \vec{k}_2 + \vec{k}_{2'}$ and $\vec{k}_{\text{out}} = -\vec{k}_1 + \vec{k}_2 + \vec{k}_{2'}$.

In a quantum mechanical description of multiwave mixing, Liouville diagrams describe the sequence of coherences and populations created by successive excitation pulses.[24] Figure 1 shows all the possible pathways for our MEOW experiment. Here, the arrows designate interactions with the excitation pulses and the letters designate the density matrix elements describing the coherences and populations resulting after each interaction. The first and second letters describe the ket and bra state, respectively, of a $|m\rangle\langle n|$ coherence or population. The boxes indicate either the ground state population (*gg*) or an emitting output coherence (e.g., *3a*,*2a)*. The arrows are not labeled with the fields creating the interactions because the interactions can be caused by different excitation fields. The experiments in this paper use three separate fields, but each field can create multiple interactions. After multiple interactions, fields with positive *k* vectors cause net ket state changes to move right in Figure 1 or bra state changes to move up. Fields with negative *k* vectors cause the opposite changes. In the strong field limit, the arrows are double-headed since forward and reverse transitions occur. The transitions created by any one field, however, are constrained by the phase-matching condition to an odd number so the net momentum matches the phase-matching condition. For example, the phase-matching has a $-\vec{k}_2$ vector for excitation pulse 2. If it interacts *N* times, the phase-matching requires $[(N - 1)/(2)]\vec{k}_2 - [(N + 1)/(2)]\vec{k}_2 = -\vec{k}_2$ and that *N* must be odd. For the conditions used in this paper, excitation pulses 2 and 2′ are temporally overlapped and pulse 1 is much weaker and delayed by 6 ps. Since pulses 2 and 2′ have opposite signs in the phase-matching, their net effect is to create a series of transitions from the ground state population to the different excited state populations. For example, one lowest order Liouville pathway that creates the 3*a*,3*a* population is

$$gg \xrightarrow{2'} ag \xrightarrow{-2'} a,a \xrightarrow{2'} 2a,a \xrightarrow{-2'} 2a,2a \xrightarrow{2'} 3a,2a \xrightarrow{-2} 3a,3a$$

but there are many other equivalent pathways that result in the same population and all must be considered. The last pulse (labeled 1) is weak and interacts only once. It interacts with the 3*a*,3*a* population and can create a 4*a*,3*a* or 3*a*,2*a* output coherence by

$$3a,3a \xrightarrow{1} 4a,3a \quad \text{or} \quad 3a,3a \xrightarrow{1} 3a,2a$$

respectively. Both output coherences result from these seventh order processes and are eight-wave mixing pathways.

The 3*a*,2*a* output coherence can also be created by a fifth order 6-wave mixing process such as

$$gg \xrightarrow{2'} ag \xrightarrow{2'} 2a,g \xrightarrow{-2'} 2a,a \xrightarrow{-2} 2a,2a \xrightarrow{1} 3a,2a$$

Since both processes are quantum mechanically equivalent, the contributions from both must be summed and will interfere. If the excitation frequencies are fully resonant, the successive odd orders have opposite signs, so the interference between successive odd orders is destructive. As a specific example, we write the density matrix elements of the output coherences for the two example Liouville pathways in the steady state limit where the excitation pulses are long compared to the dephasing time. This limit is appropriate for the experiments in this paper. The expressions are

$$\rho_{3a,2a} = \frac{\Omega_{ag}^2 \Omega_{2a,a}^2 \Omega_{3a,2a}}{32\Delta_{ag}\Delta_{2a,g}\Delta_{2a,a}\Delta_{2a,2a}\Delta_{3a,2a}} \times \rho_{gg} \mathrm{e}^{i[2\vec{k}_{2'} - \vec{k}_{2'} - \vec{k}_2 + \vec{k}_1)z - (2\omega_{2'} - \omega_{2'} - \omega_2 + \omega_1)t]} \tag{2}$$

$$\rho_{3a,2a} = \frac{\Omega_{ag}^2 \Omega_{2a,a}^2 \Omega_{3a,2a}^3}{64\Delta_{ag}\Delta_{aa}\Delta_{2a,a}\Delta_{2a,2a}\Delta_{3a,2a}\Delta_{3a,3a}\Delta_{3a,2a}} \times \rho_{gg} \mathrm{e}^{i[3\vec{k}_{2'} - 2\vec{k}_{2'} - \vec{k}_2 + \vec{k}_1)z - (3\omega_{2'} - 2\omega_{2'} - \omega_2 + \omega_1)t]} \tag{3}$$

for the fifth and seventh order processes, respectively. Here, $\Omega_{ij} \equiv (\mu_{ij}E^\circ)/(\hbar)$ is the Rabi frequency where E° is the electric field associated with the $i \leftrightarrow j$ transition; $\Delta_{ij} \equiv \omega_{ij} - \omega_{\text{lasers}} - i\Gamma_{ij}$ is the resonance detuning factor for the *ij* coherence; ω_{lasers} is the combination of excitation frequencies creating the *ij* coherence; and μ_{ij}, ω_{ij}, and Γ_{ij} are the transition moment, frequency, and dephasing rate of the *ij* coherence, respectively. The *k* vectors and excitation frequencies from each interaction are shown explicitly to reflect the order of the pathway. On resonance, eqs 2 and 3 become

$$\rho_{3a,2a} = \frac{i\Omega_{ag}^2 \Omega_{2a,a}^2 \Omega_{3a,2a}}{32\Gamma_{ag}\Gamma_{2a,g}\Gamma_{2a,a}\Gamma_{2a,2a}\Gamma_{3a,2a}} \rho_{gg} \mathrm{e}^{i[\vec{k}_{2'} - \vec{k}_2 + \vec{k}_1)z - \omega_1 t]} \tag{4}$$

and

$$\rho_{3a,2a} = -\frac{i\Omega_{ag}^2\Omega_{2a,a}^2\Omega_{3a,2a}^3}{64\Gamma_{ag}\Gamma_{aa}\Gamma_{2a,a}\Gamma_{2a,2a}\Gamma_{3a,3a}\Gamma_{3a,2a}^2}\rho_{gg}e^{i[\vec{k}_{2'}-\vec{k}_2+\vec{k}_1)z-\omega_1 t]} \quad (5)$$

so the different orders of interactions result in opposite signs for the pathways.

In addition to interference between pathways with different orders of interactions that create the same coherence, one must also consider interference between different output coherences arising from the same *N*-wave mixing process. Successively higher output coherences differ in sign because they involve different numbers of bra-side interactions. Each bra-side interaction changes the sign of the nonlinear polarization. For example, the *ag* and 3*a*,2*a* coherences involve an even number of bra-side transitions and constructively interfere while they destructively interfere with the 2*a*,*a* and 4*a*,3*a* coherences, which have an odd number of bra-side interactions.

The experiments reported in this paper involve electric fields that are intense enough that dynamic Stark effects become important. The dynamic Stark effect can be conceptualized as a breakdown of the Taylor series perturbative expansion.[25,26] As the excitation intensity increases, the higher order coherences and populations become important and the complex interference effects mentioned above come fully into play. Ultimately, the vibrational transitions split and widen. In the steady state limit of a closed two-state system, the dynamic Stark effect causes the following well-known relationship:[25−27]

$$\rho_{ag} = \frac{\Omega\Gamma_{aa}\Delta_{ag}^*}{2(\Gamma_{aa}|\Delta_{ag}|^2 + \Gamma_{ag}\Omega^2)}\rho_{gg}^{\circ} \quad (6)$$

The amount of broadening will therefore depend on $[(\Gamma_{ag})/(\Gamma_{aa})]^{1/2}\Omega$. Our typical experimental conditions are 1 μJ pulse energy, 1 ps pulse width, 50 μm beam waist, and a 0.9 D transition dipole moment. The corresponding Rabi frequency is ~40 cm^{-1} so the dynamic Stark effect becomes important. In addition, as higher levels in the potential well are excited, lifetimes drop and transition dipole moments increase. The higher transition moment will increase the Rabi frequency for these excited state transitions but the importance of the dynamic Stark effect will depend on the Γ_{ag}/Γ_{aa} ratio, which may become smaller. We believe that the high Rabi frequency, the large Γ_{ag}/Γ_{aa} ratio, and the increased sensitivity of these frequency domain methods permits reaching overtone states with anharmonicities that are outside the excitation pulse bandwidth and permit the identification of the fifth overtone state.

In order to model experimental observations, all participating pathways must be considered together. In perturbative simulations, creation of any output coherence requires a minimum number of interactions, but it can also be created by an infinite number of interactions beyond the minimum. Clearly, the perturbative approach fails in the limit of strong fields. It will be important to develop nonperturbative simulation approaches for quantitatively describing the data reported in this paper.[28,29] Further modeling of the MEOW spectroscopy is not attempted because of the complexity of the pathways that must be considered and the difficulties in treating the simulations nonperturbatively.

Experiment

A commercial Ti:sapphire oscillator/regenerative amplifier creates ~1 ps pulses at 1 kHz, and 1.2 W power. The pulse train is divided and excites two independently tunable optical parametric amplifiers (OPAs). Difference frequency generation from the OPA signal and idler create tunable mid-IR light. One OPA creates the ω_1 beam, and the second OPA output is divided to create the ω_2 and $\omega_{2'}$ beams. Typical energies in our experiments range from 0.2 to 1.5 μJ for ω_1 and 2.3 and 1.2 μJ for ω_2 and $\omega_{2'}$, respectively. The spectral width (fwhm) is 20 cm^{-1}. The spectral output also has two satellite features that are <1% of the central feature and shifted by 27 cm^{-1}. Computer-controlled delay lines determine the temporal delays between the ω_i and ω_j pulses, $\tau_{ij} = \tau_i - \tau_j$. The beams are focused into the sample with a 10 cm focal length off-axis parabolic mirror. A second off-axis parabolic mirror collimates the signal beam. The signal in the $\vec{k}_{\text{out}} = \vec{k}_1 - \vec{k}_2 + \vec{k}_{2'}$ or $\vec{k}_{\text{out}} = -\vec{k}_1 + \vec{k}_2 + \vec{k}_{2'}$ phase-matching direction is isolated with an iris, sent to a 0.3 m monochromator, and detected with a single element mercury cadmium telluride detector. A boxcar integrator resolves the signal that is then digitized with a 12-bit data acquisition card. Step sizes in our scans are 2 cm^{-1} for frequency scans, and 0.2 ps for temporal scans. Each data point is the average of 2000 laser shots.

The sample consisted of a 125 μm thick 0.5 mM solution of $W(CO)_6$ in hexane held between 2 mm CaF_2 windows. The resulting absorbance is <1 for the T_{1u} carbonyl mode at 1983 cm^{-1}. The transition dipole moment for this vibrational mode has been reported as ~1 D in the literature.[4] Our measurements indicate 0.8 D.

Results and Discussion

Figure 2 shows the dependence of the signal intensity on the excitation lasers pulse energy when the laser and monochromator frequencies were tuned to the $W(CO)_6$ fundamental at 1983 cm^{-1}. For Figure 2a, the energy of the ω_2 and $\omega_{2'}$ excitation pulses were attenuated with irises to 0.107 and 0.058 μJ/pulse, respectively, while changing the energy of ω_1 with an iris. The signal intensity depends linearly on the ω_1 excitation pulse energy as expected for a four-wave mixing signal in this phase-matching geometry. The dependence departs from linear when the ω_1 energy reaches 0.7 μJ and then decreases at higher energies. This change reflects the importance of higher order processes that interfere with the four-wave mixing. Figure 2b shows a log−log plot when ω_1 was attenuated via an iris to ~0.25 μJ, and the $\omega_2/\omega_{2'}$ beam powers were adjusted by a polarizer pair. The polarizers were inserted before dividing the OPA output into ω_2 and $\omega_{2'}$, so both beams increased proportionally. At low intensities, the signal intensity increases quadratically with a slope of two as expected for the four-wave mixing phase-matching condition. At higher intensities, the signal intensity saturates and becomes independent of the ω_2 intensity.

Figure 3 shows the logarithmic dependence of the T_{1u} mode signal intensity on the excitation frequencies with the constraint that the monochromator frequency $\omega_m = \omega_1$. To prevent high order processes, all pulse energies were between 0.1 and 0.3 μJ. The ω_1 beam was attenuated with a polarizer pair, and the $\omega_2/\omega_{2'}$ beams were attenuated with a series of irises. The time ordering of the pulses was such that ω_2 and $\omega_{2'}$ are temporally overlapped, and they arrive 6 ps before ω_1. Phase-matching requires that the first two interactions produce a population. The third pulse probes the population. The peak located at $(\omega_1, \omega_2) = (1983, 1983)$ cm^{-1} is the diagonal peak that is created by the coherence pathways shown as wave mixing energy level (WMEL)[30] diagrams in Figures 4a−d. The peak at $(\omega_1, \omega_2) = (1968, 1983)$ cm^{-1} is formed by the pathways shown in Figures

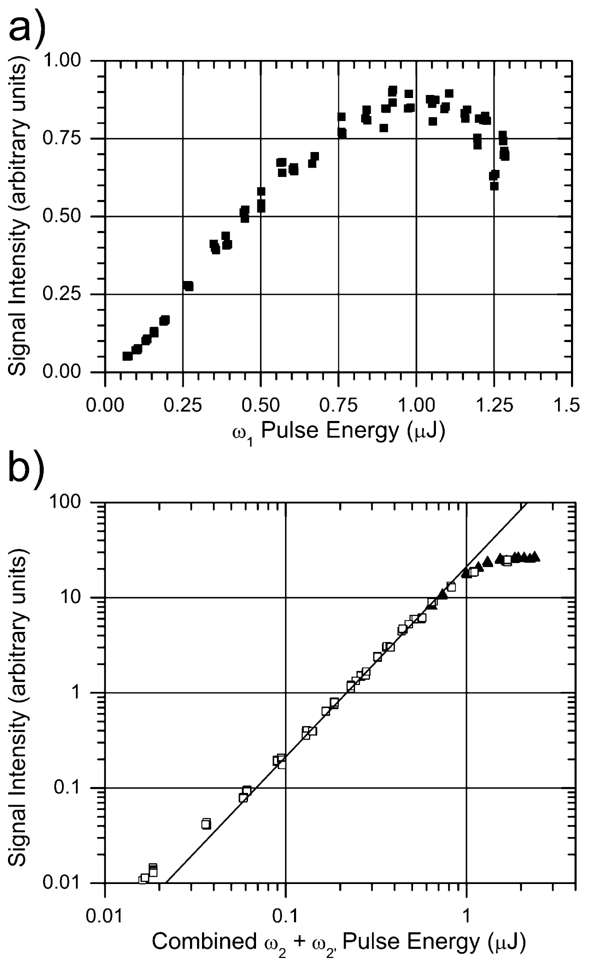

Figure 2. Dependence of the output intensity on the excitation energy. (a) Adjusted ω_1 intensity for $\tau_{21} = 0.0$ ps and $\tau_{2'1} = 5.0$ ps. ω_2 and $\omega_{2'}$ excitation energies were ~0.107 and 0.058 μJ/pulse, respectively. (b) Adjusted ω_2 and $\omega_{2'}$ intensity for $\tau_{21} = \tau_{2'1} \approx -5.0$ ps. ω_1 intensity ~0.22 μJ/pulse for the open squares, and ~0.3 μJ/pulse for the solid triangles. The two symbols represent two data sets that were scaled for differences in excitation beam overlap and ω_1 intensity. A line with a slope of two is shown in the figure.

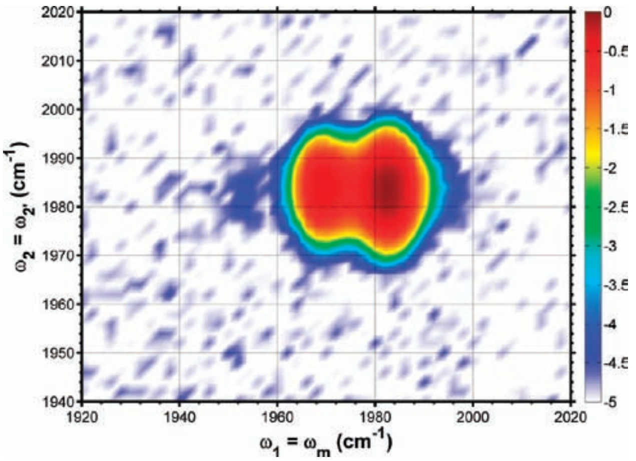

Figure 3. Dependence of the output intensity on the excitation frequencies ω_1 and ω_2. The monochromator frequency was synchronously scanned so $\omega_m = \omega_1$ and the excitation time delays were fixed at $\tau_{21} = \tau_{2'1} = -6.0$ ps. The excitation energies were low. The color bar is logarithmic.

4e−f. While ω_2 and $\omega_{2'}$ are still tuned to the fundamental mode for this second peak, the final laser ω_1 and the signal frequency ω_m correspond to the overtone transition. These peaks are separated by their anharmonicity. Finally, there is a third peak at $(\omega_1, \omega_2) = (1954, 1983)$ cm^{-1}. This peak results from a six-wave mixing pathway shown in Figure 4g that involves the second overtone. Its position reflects the additional anharmonicity of the second overtone. It becomes much brighter at higher excitation intensities.

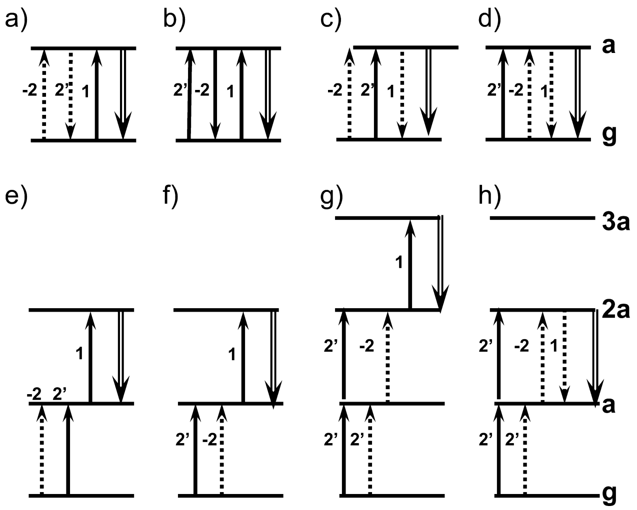

Figure 4. Wave mixing energy level (WMEL) diagrams[30] for representative nonlinear processes. The solid and dotted arrows show ket- and bra-side interactions with fields labeled by numbers, and the double arrow shows the output field.

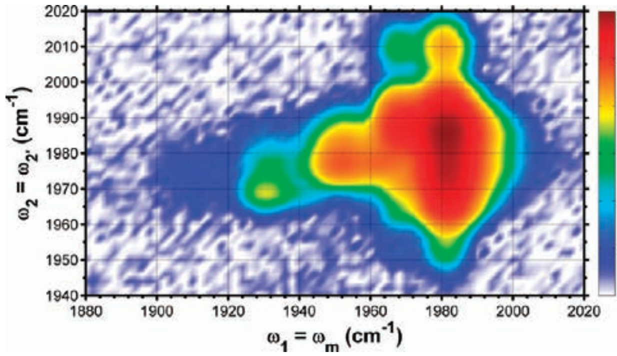

Figure 5. Dependence of the output intensity on the excitation frequencies ω_1 and ω_2. The monochromator frequency was synchronously scanned so $\omega_m = \omega_1$ and the excitation time delays were fixed at $\tau_{21} = \tau_{2'1} = -6.0$ ps. The ω_1 energy was low and the ω_2 energy was high. The color bar is logarithmic.

Figure 5 is the same scan as Figure 3, but the power of the ω_2 and $\omega_{2'}$ laser beams have increased to 2.25 and 1.25 μJ, respectively. The fundamental peak has broadened significantly along the ω_2 axis. In Figure 3, the full width at 10^{-5} of the maximum intensity was 35 cm^{-1} along the *y*-axis; at high power it is 70 cm^{-1}. The satellite lobes near 2010 and 1955 cm^{-1} are attributed to excitation of the T_{1u} mode by the weak satellite features in the excitation pulses. These satellites appear anomalously bright relative to the T_{1u} peak at 1983 cm^{-1} because the T_{1u} intensity is saturated at high excitation intensities by the aforementioned interference with higher order processes. While the 1983 cm^{-1} peak is somewhat broader along the ω_1 dimension, it is not broadened appreciably for two reasons. First, the monochromator frequency at $\omega_m = \omega_1$ measures the free induction decay of the output coherence and thus provides spectral narrowing. Second, the probe pulse is weak and delayed by 6 ps so dynamic Stark effects are not as important.

There are new peaks that are red-shifted from those observed in the low intensity spectrum in Figure 3. Figures 4g−h show

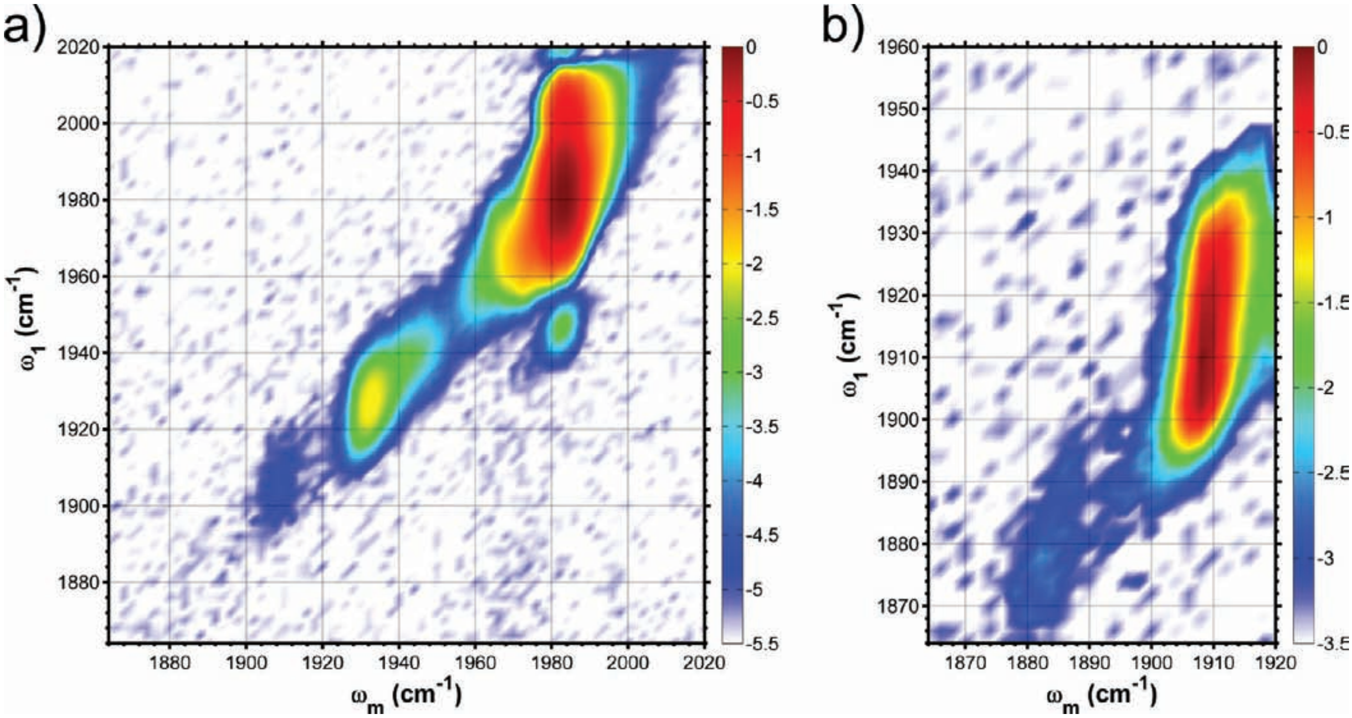

Figure 6. Dependence of the output intensity on the ω_1 excitation frequency and the monochromator frequency, ω_m. The ω_2 excitation frequency was (a) 1974 cm^{-1} and (b) 1970 cm^{-1}, and the excitation time delays were fixed at $\tau_{21} = \tau_{2'1} = -6.0$ ps. The ω_1 energy was low and the ω_2 energy was high. The color bar is logarithmic.

two example WMEL diagrams that involve the second and first overtone transitions, respectively. These peaks result from higher order processes involving more energetic overtone states. The red shifting along the ω_1 dimension directly corresponds to the changes in the free induction decay frequencies of coherences involving these higher overtone states. These peaks also demonstrate a steady red shifting along the ω_2 dimension. To have output at the third overtone (3*a*,2*a* coherence), the initial ω_2 and $\omega_{2'}$ excitations must create a population in either the 2*a* or 3*a* state. Since ω_2 and $\omega_{2'}$ have identical frequencies, the optimal position for creating populations in the second overtone will be a compromise frequency between the $\omega_{g,a}$ and $\omega_{a,2a}$ transition frequencies. Though dynamic Stark effects make the determination of the optimum excitation frequencies complex, a slight but steady trend of higher order processes being optimized by red shifting the ω_2 frequency is clear. The advantage of shifting the central excitation frequency has also been previously demonstrated with chirped pulses[5] and pulse shapers.[7] By simply changing the frequency of the $\omega_2/\omega_{2'}$ laser, we can also optimize various pathways and preferentially enhance particular peaks.

Although the peak locations for the fundamental and first overtone are clear in the low power scan of Figure 2, several overtones in the high power scan are obscured by interference effects from neighboring peaks. In order to improve the resolution, we set ω_2 to a frequency that optimizes the desired high-order peaks and scanned ω_1 versus ω_m. Figure 6 shows the results of this experiment. Figure 6b repeats the spectrum in Figure 6a but with $\omega_2 = 1970$ cm^{-1} so the higher order overtone features are emphasized. Note that the peaks are slightly slanted with slopes of $(\mathrm{d}\omega_1)/(\mathrm{d}\omega_m) = 6$. The slant results because the monochromator measures both the free induction decay that always appears at the frequency of the output coherence and the driven nonlinear polarization that appears at $\omega_m = \omega_1$. The slope depends on the relative importance of the two processes. The center position of ω_m for each feature in Figure 6 defines the frequency of each overtone state. We determined the centers by fitting Gaussian line-shapes to spectra where ω_2 was centered on each feature and ω_1 varied across the line-shape. Table 1 summarizes these frequencies and compares them to previously reported literature values. This approach minimizes the effects of interference between the different output coherences that can shift the positions if the 2D spectrum of Figure 6 is projected onto the ω_m dimension and integrated.

Table 1

quantum number	transition frequency (cm^{-1}), This work	calculated value[a]	transition frequency (cm^{-1}), Literature
1	1983	1982.5	1982[4,6]
2	1968	1969.4	1967,4 1966[6]
3	1954	1953.0	1952,4 1951[6]
4	1934	1933.3	1933,4 1930[6]
5	1909	1910.1	1907[6]
6	1884	1883.6	1882[6]

[a] $\omega_0 = 1998.7$ cm^{-1}, $a = 2.332$ cm^{-1}, $b = 0.5595$ cm^{-1}.

In Figure 7, we fit the observed levels with the following modified Morse potential containing a cubic anharmonicity term.[31]

$$E_v = \bar{\omega}_e\left(v + \frac{1}{2}\right) - a\left(v + \frac{1}{2}\right)^2 - b\left(v + \frac{1}{2}\right)^3 \qquad (7)$$

It was necessary to add the cubic term in order to obtain agreement with the measured values. The fitting parameters for the transition frequencies are summarized in Table 1.

Figure 8 shows representative temporal dependences of the high overtone state dynamics. Interpretation of the temporal dependences has been covered in previous publications for four-wave mixing.[32,33] Scans along the diagonal for negative $\tau_{21} = \tau_{2'1}$ measure the population relaxation rate, while scans over positive values measure the coherence dephasing rates. Figure

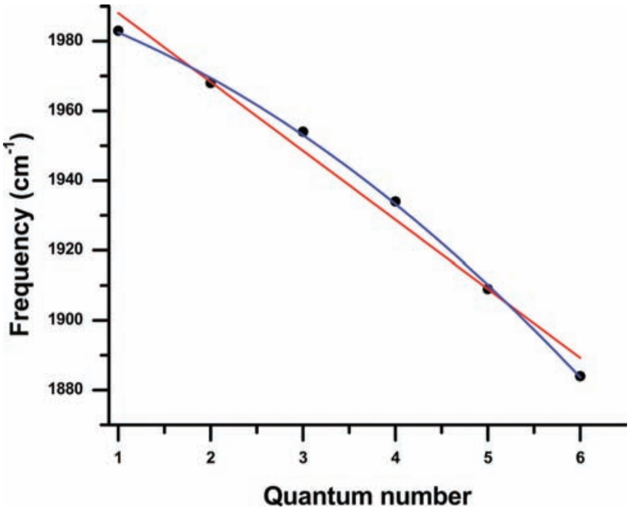

Figure 7. Dependence of the transition frequency on the quantum number of the overtone state. The red line represents a Morse potential, and the blue line includes an additional third-order anharmonicity.

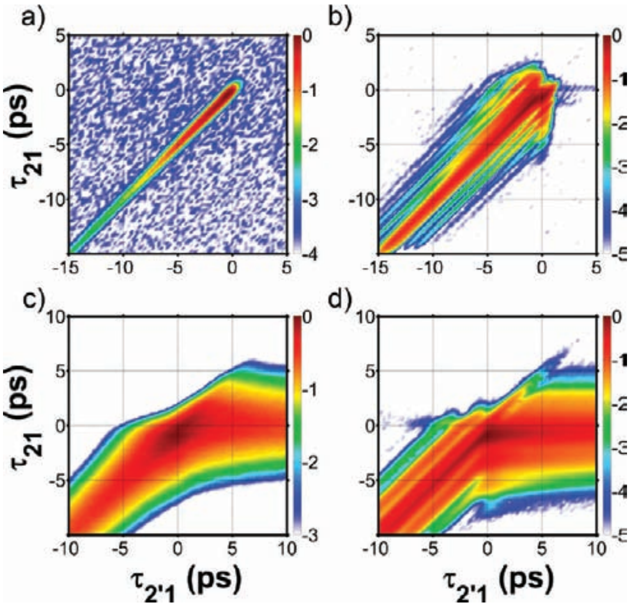

Figure 8. Dependence of the output intensity on the temporal excitation pulse delays, τ_{21} and $\tau_{2'1}$ for fixed excitation and monochromator frequencies. (a) $\omega_1 = 1884$ cm^{-1}, $\omega_2 = 1965$ cm^{-1}, $\omega_m = 1883$ cm^{-1}. The ω_1 energy was low and the ω_2 energy was high. The intensity color bar is logarithmic. (b) $\omega_1 = 1934$ cm^{-1}, $\omega_2 = 1974$ cm^{-1}, $\omega_m = 1934$ cm^{-1}. The ω_1 energy was low and the ω_2 energy was high. The intensity color bar is logarithmic. (c) $\omega_1 = 1983$ cm^{-1}, $\omega_2 = 1983$ cm^{-1}, $\omega_m = 1983$ cm^{-1}. The ω_1 and ω_2 energies were low. The plot retains its shape for output intensities 3 orders of magnitude lower than those show. The intensity color bar is logarithmic. (d) $\omega_1 = 1983$ cm^{-1}, $\omega_2 = 1983$ cm^{-1}, $\omega_m = 1983$ cm^{-1}. The ω_1 was low and ω_2 energy was high. The intensity color bar is logarithmic.

8a shows the temporal dependence of the $v = 6$ overtone at 1883 cm^{-1}. As expected, signal appears only when the first two lasers are temporally overlapped and create populations. Population relaxation causes the intensity to decay for increasingly negative values of $\tau_{21} = \tau_{2'1}$. Signal is only observed near $\tau_{21} = \tau_{2'1}$ because the two most intense excitation pulses must be temporally overlapped to create sufficiently high Rabi frequencies to populate the $v = 5$ overtone state. Figure 8b shows the same scan, but the excitation frequencies excite the $v = 4$ overtone. Moving along the diagonal again measures the population relaxation. Here, the dephasing of the coherences can also be measured from the intensity decay along $\tau_{2'1}$ or τ_{21} since the coherence dephasing rates are slow enough to observe their dynamics and the first two excitations can populate the $v = 3$ state without being temporally overlapped. Figures 8c−d show the dynamics of the $v = 1$ state at low excitation intensities and high ω_2 energies, respectively. The $v = 1$ dynamics differs from the others because $\omega_1 = \omega_2$ for this state, so the $v = 1$ population can be excited regardless of whether the ω_1 excitation occurs before or after the other excitation events. The coherence dephasing rate is sufficiently slow that it is also resolved. At higher ω_2 intensity, additional modulations appear in the dynamics, again because of beating between the different coherences that are broadened by the dynamic Stark effect. The broadening results in spectral overlap so the different pathways interfere and create the modulations. We have also measured the dynamics for the $v = 2$, 3, and 5 overtones, and these are provided in the Supporting Information.

We also present preliminary results for MEOW methods using the $\vec{k}_{\mathrm{out}} = -\vec{k}_1 + \vec{k}_2 + \vec{k}_{2'}$ phase-matching condition. This phase-matching condition has the advantage that the output frequency is different from the excitation frequencies (assuming $\omega_1 \neq \omega_2$) so scattered light is not as important. Previously, we used this phase-matching condition for the observation of coherence transfer when cross-peaks are excited.[34] The phase-matching condition for cross-peaks results in output coherences with forbidden transitions,[35] but they become allowed if coherence transfer occurs. In this paper, however, there are no cross-peaks since W(CO)$_6$ has only a single CO vibrational stretching mode. For this case, the output coherences have allowed transitions. This phase-matching condition is fully coherent if the ω_2 and $\omega_{2'}$ beam precede the ω_1 beam so there are no intermediate populations. The last pulse then acts as a probe that is independently tunable from the previous excitation frequencies. For example, the first two excitations in four-wave mixing create a $2a,g$ double quantum coherence. The third beam then creates either a $2a,a$ or ag output coherence. If the first two beams create n interactions in an $n + 2$ wave mixing experiment, the phase-matching condition requires that n is even and the sum of two odd numbers representing the interactions for the two beams. These interactions will create a series of multiple quantum coherences of which the most energetic coherence will be $(n/2 + 1)a$, $(n/2 - 1)a$. A bra- or ket-side interaction with the last pulse then creates the $(n/2 + 1)a$, $(n/2)a$ or $(n/2)a$, $(n/2 - 1)a$ output coherence. The result will be a series of peaks in the two-dimensional spectrum with ω_m and ω_1 matching the $n/2$ and $n/2 - 1$ overtone frequencies, respectively, or vice versa.

Figure 9 shows the spectra for the phase-matching condition $\vec{k}_{\mathrm{out}} = -\vec{k}_1 + \vec{k}_2 + \vec{k}_{2'}$ at low excitation intensity (Figure 9a) and high ω_2 intensity (Figure 9b). For these spectra, $\omega_2 = 1978$ cm^{-1} and ω_1 and ω_m are scanned. The delays are $\tau_{21} = \tau_{2'1} = -2.0$ ps so the first two excitation pulses created a series of coherences between overtones. The output frequency for the driven process appears at $\omega_{\mathrm{out}} = 2\omega_2 - \omega_1$ so the driven output frequency will change as $(d\omega_1)/(d\omega_m) = -1$. The slope gives the spectrum an asymmetrical shape. Figure 9a has two peaks corresponding to the two WMEL diagrams drawn near each peak. At higher intensity, additional structure appears in the spectrum from the higher order wave mixing effects. The circles appear at the positions expected for the peaks formed by n interactions of the first two excitation pulses. Clearly, the dynamic Stark effects create more structure in the spectrum than can be explained by the simple arguments presented here. Additional data showing the dependence of the signal intensity on the two excitation frequencies and the dependence on the

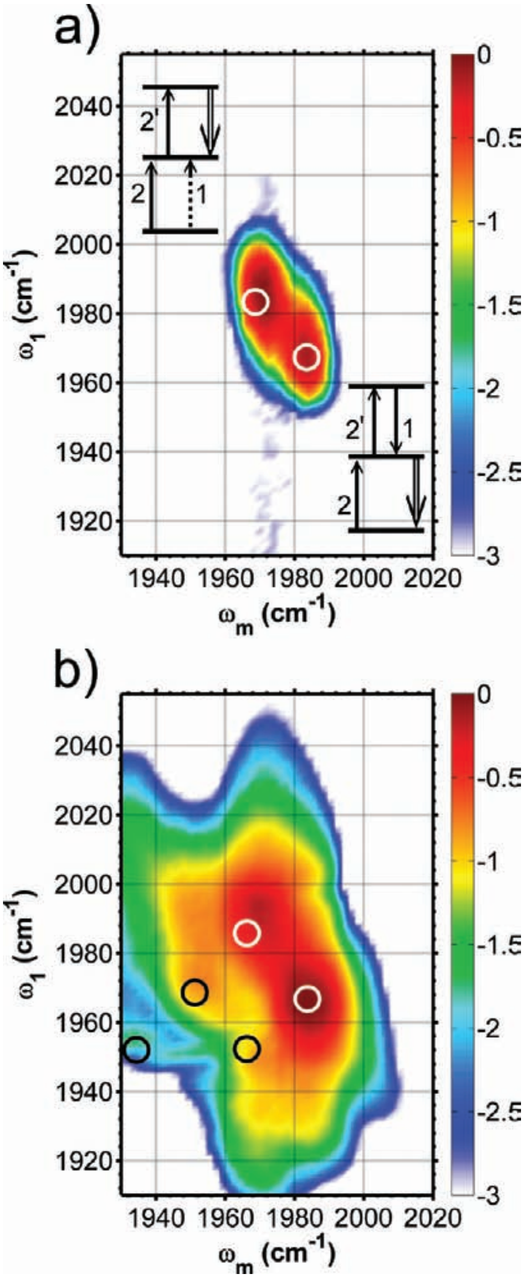

Figure 9. Dependence of the output intensity on the ω_1 excitation frequency and the ω_m monochromator frequency for the $\vec{k}_4 = -\vec{k}_1 + \vec{k}_2 + \vec{k}_{2'}$ phase-matching geometry. The ω_2 excitation frequency was 1978 cm^{-1} and the excitation time delays were fixed at $\tau_{21} = \tau_{2'1} = -2.0$ ps. The excitation energies were (a) low for all beams or (b) high for all beams. The color bar is logarithmic.

temporal delay times appears in the Supporting Information. Further work has not been done on this phase-matching condition.

Conclusions

Coherent multidimensional spectroscopy (CMDS) has relied on four-wave mixing methods such as stimulated photon echo, pump–probe, and transient grating processes.[36] It will be interesting to extend CMDS methods to higher order multiwave mixing because increasing the number of interactions can increase the spectral selectivity of CMDS methods. The higher excitation intensities required to create multiwave mixing also create dynamic Stark effects. This work studied the influence of dynamic Stark effects on the coherent multidimensional vibrational spectra of $W(CO)_6$ as a way to isolate the dynamic Stark effect from other influences. Two tunable excitation frequencies and three excitation beams created output coherences using multiply enhanced odd-order wave-mixing spectroscopy and a monochromator measured the free induction decay and driven emission of the output coherences. Raising the excitation intensity created new features in two-dimensional spectra acquired by scanning different combinations of the excitation and monochromator frequencies. The new features were produced by higher order nonlinear processes involving an odd number of interactions with the excitation fields. The free induction decay frequency measured the anharmonicity of the different overtone states up to $v = 6$. It will be important to develop nonperturbative simulation methods that can provide a quantitative model of the multidimensional spectroscopy so it becomes feasible to extract more molecular information about the potential energy surface and the coherent dynamics that control the spectroscopy as well as deconvolute the effects of interference between multiple coherence pathways.[28,29]

$W(CO)_6$ is a model compound that is not representative of the broader class of electronic and vibrational transitions. Electronic and vibrational transitions have different transition moments and multiple quantum states that are not spectrally isolated. Typical vibrational transition moments are 15× smaller ($\mu \approx 0.06$ D for $\epsilon \approx 100$ L/mol cm) than $W(CO)_6$ so the corresponding Rabi frequencies would be ~3 cm^{-1}. Such Rabi frequencies are comparable to typical vibrational dephasing rates so dynamic Stark effects must still be considered. In addition, the excitation intensity can be raised by tighter focusing if larger dynamic Stark effects are required. The dynamic Stark effects have two consequences: (1) they allow ladder-climbing transitions within a specific mode; (2) they make higher order mixing processes comparable in efficiency to lower order processes. Ladder-climbing transitions allow probing of the higher energy parts of molecular potential energy surfaces while creating higher order mixing processes allow the use of multiple excitation frequencies that can excite multiple quantum states in multistate samples. If dynamic Stark effects occur for multiple state excitations, it becomes possible to probe the off-diagonal parts of the molecular potential energy surface.

The multiple transitions in $W(CO)_6$ create a series of populations in successively higher states. The states in $W(CO)_6$ have long population lifetimes so population relaxation is not important for the experiments reported here.[4] However, in molecules with shorter population lifetimes, population relaxation will result in additional relaxation assisted[37] coherence pathways that cause new spectral features to appear at longer population delay times. These effects will cause spectral congestion and make interpretation more difficult. The relaxation assisted pathways can be eliminated by using fully coherent pathways in samples with multiple quantum states. We have shown that mixed frequency/time domain CMDS can create multiple quantum coherences involving fully coherent pathways that lack the intermediate populations that undergo population relaxation.[38] The resulting spectra then do not contain relaxation assisted features.

This work is also applicable to CMDS of electronic transitions where the transition moments are comparable or larger than those of $W(CO)_6$. The importance of dynamic Stark effects will depend on the dephasing rates for the electronic transitions. There are many examples of nonlinear experiments with electronic states where saturation and dynamic Stark effects become important so MEOW spectroscopy should be applicable to these systems as well.

Future directions for this work will explore using dynamic Stark effects and fully coherent pathways involving multiple quantum state coherences for molecular spectroscopy in more complex systems. The multiple quantum state coherences will provide spectral selectivity in much the same way as multiple pulse NMR methods such as heteronuclear multiple quantum coherence (HMQC) spectroscopy.[39] The dynamic Stark effects will probe the diagonal and off-diagonal parts of the molecular potential energy surface. The use of mixed frequency/time domain methods is particularly well-suited for this approach. Since these methods require only short-term phase coherence, it is possible to use independent excitation pulses to create multiple quantum coherences involving states with disparate energies.[32]

Acknowledgment. This work was supported by the National Science Foundation under grant CHE-0650431.

Supporting Information Available: The Supporting Information contains figures for the temporal dependence of the second, third, and fifth overtone states on the excitation pulse time delays and figures for the excitation frequency dependence of the output coherences when $\omega_m = \omega_2$ for the phase matching and when there is no monochromator. This material is available free of charge via the Internet at http://pubs.acs.org.

References and Notes

(1) Clore, G. M.; Gronenborn, A. M. *Science* **1991**, *252*, 1390.

(2) Bax, A.; Delaglio, F.; Ikura, M.; Kay, L. E.; Clore, M.; Gronenborn, A.; Torchia, D. *Abstr. Pap. Am. Chem. Soc.* **1991**, *202*, 113.

(3) Wuthrich, K. *Science* **1989**, *243*, 45.

(4) Arrivo, S. M.; Dougherty, T. P.; Grubbs, W. T.; Heilweil, E. J. *Chem. Phys. Lett.* **1995**, *235*, 247.

(5) Kleiman, V. D.; Arrivo, S. M.; Melinger, J. S.; Heilweil, E. J. *Chem. Phys.* **1998**, *233*, 207.

(6) Witte, T.; Yeston, J. S.; Motzkus, M.; Heilweil, E. J.; Kompa, K. L. *Chem. Phys. Lett.* **2004**, *392*, 156.

(7) Strasfeld, D. B.; Shim, S. H.; Zanni, M. T. *Phys. Rev. Lett.* **2007**, *99*, 038102.

(8) Rector, K. D.; Fayer, M. D.; Engholm, J. R.; Crosson, E.; Smith, T. I.; Schwettman, H. A. *Chem. Phys. Lett.* **1999**, *305*, 51.

(9) Myers, D. J.; Chen, S.; Shigeiwa, M.; Cherayil, B. J.; Fayer, M. D. *J. Chem. Phys.* **1998**, *109*, 5971.

(10) Rector, K. D.; Fayer, M. D. *J. Chem. Phys.* **1998**, *108*, 1794.

(11) Myers, D. J.; Urdahl, R. S.; Cherayil, B. J.; Fayer, M. D. *J. Chem. Phys.* **1997**, *107*, 9741.

(12) Rector, K. D.; Kwok, A. S.; Ferrante, C.; Tokmakoff, A.; Rella, C. W.; Fayer, M. D. *J. Chem. Phys.* **1997**, *106*, 10027.

(13) Rector, K. D.; Fayer, M. D. *Mol. Cryst. Liq. Cryst. Sci. Technol. A* **1996**, *291*, 1.

(14) Tokmakoff, A.; Zimdars, D.; Urdahl, R. S.; Francis, R. S.; Kwok, A. S.; Fayer, M. D. *J. Phys. Chem.* **1995**, *99*, 13310.

(15) Moore, P.; Tokmakoff, A.; Keyes, T.; Fayer, M. D. *J. Chem. Phys.* **1995**, *103*, 3325.

(16) Tokmakoff, A.; Fayer, M. D. *J. Chem. Phys.* **1995**, *103*, 2810.

(17) Tokmakoff, A.; Kowk, A.; Urdahl, R.; Zimdars, D. A.; Francis, R.; Fayer, M. D. *Laser Phys.* **1995**, *5*, 652.

(18) Tokmakoff, A.; Kowk, A.; Urhdal, R.; Zimdars, D. A.; Fayer, M. D. *Nucl. Instrum. Methods Phys. Res. Sect. A* **1995**, *358*, 540.

(19) Tokmakoff, A.; Kwok, A. S.; Urdahl, R. S.; Francis, R. S.; Fayer, M. D. *Chem. Phys. Lett.* **1995**, *234*, 289.

(20) Tokmakoff, A.; Zimdars, D.; Sauter, B.; Francis, R. S.; Kwok, A. S.; Fayer, M. D. *J. Chem. Phys.* **1994**, *101*, 1741.

(21) Tokmakoff, A.; Sauter, B.; Kwok, A. S.; Fayer, M. D. *Chem. Phys. Lett.* **1994**, *221*, 412.

(22) Zimdars, D.; Tokmakoff, A.; Chen, S.; Greenfield, S. R.; Fayer, M. D.; Smith, T. I.; Schwettman, H. A. *Phys. Rev. Lett.* **1993**, *70*, 2718.

(23) Wright, J. C.; Carlson, R. J.; Hurst, G. B.; Steehler, J. K.; Riebe, M. T.; Price, B. B.; Nguyen, D. C.; Lee, S. H. *Int. Rev. Phys. Chem.* **1991**, *10*, 349.

(24) Wright, J. C. *Int. Rev. Phys. Chem.* **2002**, *21*, 185.

(25) Winker, B. K.; Wright, J. C. *Anal. Chem.* **1988**, *60*, 2599.

(26) Ouellette, F.; Denariez-Roberge, M. M. *Can. J. Phys.* **1982**, *60*, 877.

(27) Moody, S. E.; Lambropoulos, M. *Phys. Rev. A* **1977**, *15*, 1497.

(28) Cheng, Y. C.; Engel, G. S.; Fleming, G. R. *Chem. Phys.* **2007**, *341*, 285.

(29) Gelin, M. F.; Egorova, D.; Domcke, W. *J. Chem. Phys.* **2005**, *123*, 164112.

(30) Lee, D.; Albrecht, A. C. *Advances in Infrared and Raman Spectroscopy*, 1st ed.; Wiley-Heyden: Chichester, 1985; Vol. 12.

(31) Steinfel, Ji; Zare, R. N.; Jones, L.; Lesk, M.; Klempere, W. *J. Chem. Phys.* **1965**, *42*, 25.

(32) Pakoulev, A. V.; Rickard, M. A.; Meyers, K. A.; Kornau, K.; Mathew, N. A.; Thompson, D. C.; Wright, J. C. *J. Phys. Chem. A* **2006**, *110*, 3352.

(33) Pakoulev, A. V.; Rickard, M. A.; Kornau, K.; Mathew, N. A.; Yurs, L. A.; Block, S. B.; Wright, J. C. *Acc. Chem. Res.* **2009**, *42* (9), 1310.

(34) Rickard, M. A.; Pakoulev, A. V.; Mathew, N. A.; Kornau, K. M.; Wright, J. C. *J. Phys. Chem. A* **2007**, *111*, 1163.

(35) Meyer, K. A.; Besemann, D. M.; Wright, J. C. *Chem. Phys. Lett.* **2003**, *381*, 642.

(36) Mukamel, S. *Ann. Rev. Phys. Chem.* **2000**, *51*, 691.

(37) Kurochkin, D. V.; Naraharisetty, S. R. G.; Rubtsov, I. V. *Proc. Natl. Acad. Sci. U.S.A.* **2007**, *104*, 14209.

(38) Mathew, N. A.; Yurs, L. A.; Block, S. B.; Pakoulev, A. V.; Kornau, K. M.; Wright, J. C. *J. Phys. Chem. A* **2009**, *113*, ASAP.

(39) Mandal, P. K.; Majumdar, A. *Concepts Magn. Reson., Part A* **2004**, *20A*, 1.

JP905796Y